applied sciences

MDPI

Article

Experimental Investigation of a H_2O_2 Hybrid Rocket with Different Swirl Injections and Fuels

Manuel Stella [1], Lucia Zeni [1], Luca Nichelini [1], Nicolas Bellomo [1], Daniele Pavarin [1,2], Mario Tindaro Migliorino [3], Marco Fabiani [3], Daniele Bianchi [3], Francesco Nasuti [3], Christian Paravan [4], Luciano Galfetti [4], Attilio Cretella [5], Rocco Carmine Pellegrini [6], Enrico Cavallini [6] and Francesco Barato [2,*]

[1] Technology for Propulsion and Innovation S.p.A. (T4i), Via Emilia 15, 35043 Monselice, Italy; m.stella@t4innovation.com (M.S.); l.zeni@t4innovation.com (L.Z.); l.nichelini@t4innovation.com (L.N.); n.bellomo@t4innovation.com (N.B.); d.pavarin@t4innovation.com (D.P.)
[2] Department of Industrial Engineering (DII), University of Padova, Via Venezia 1, 35131 Padova, Italy
[3] Centro di Ricerca Aerospaziale Sapienza (CRAS), Sapienza University of Rome, Via Eudossiana 18, 00184 Rome, Italy; mariotindaro.migliorino@uniroma1.it (M.T.M.); m.fabiani@uniroma1.it (M.F.); daniele.bianchi@uniroma1.it (D.B.); francesco.nasuti@uniroma1.it (F.N.)
[4] Space Propulsion Laboratory (SPLab), Politecnico di Milano, Via La Masa 34, 20156 Milan, Italy; christian.paravan@polimi.it (C.P.); luciano.galfetti@polimi.it (L.G.)
[5] AVIO S.p.A., Via Latina, 00034 Colleferro, Italy; attilio.cretella@avio.com
[6] Italian Space Agency (ASI), Via del Politecnico s.n.c., 00133 Rome, Italy; rocco.pellegrini@asi.it (R.C.P.); enrico.cavallini@asi.it (E.C.)
* Correspondence: francesco.barato@unipd.it; Tel.: +39-0498079523

Abstract: Hybrid rockets have very interesting characteristics like simplicity, reliability, safety, thrust modulation, environmental friendliness and lower costs, which make them very attractive for several applications like sounding rockets, small launch vehicles, upper stages, hypersonic test-beds and planetary landers. In recent years, advancements have been made to increase hybrid motor performance, and two of the most promising solutions are vortex injection and paraffin-based fuels. Moreover, both technologies can be also used to tailor the fuel regression rate, in the first case varying the swirl intensity, and in the second case with the amount and type of additives. In this way, it is possible not only to design high-performing hybrid motors, but also to adjust their grain and chamber geometries to different mission requirements, particularly regarding thrust and burning time. In this paper, the knowledge about these two technical solutions and their coupling is extended. Three sets of experimental campaigns were performed in the frame of the Italian Space Agency-sponsored PHAEDRA program. The first one investigated a reference paraffin fuel with axial and standard vortex injection. The second campaign tested vortex injection with low values of swirl numbers down to 0.5 with a conventional plastic fuel, namely polyethylene. Finally, the last campaign tested another, lower regressing, paraffin-based fuel with the same low swirl numbers as the second campaign.

Keywords: hybrid rockets; vortex injection; paraffin-based fuels; regression rate tailoring; low swirl numbers

check for updates

Citation: Stella, M.; Zeni, L.; Nichelini, L.; Bellomo, N.; Pavarin, D.; Migliorino, M.T.; Fabiani, M.; Bianchi, D.; Nasuti, F.; Paravan, C.; et al. Experimental Investigation of a H_2O_2 Hybrid Rocket with Different Swirl Injections and Fuels. *Appl. Sci.* **2024**, *14*, 5625. https://doi.org/10.3390/app14135625

Academic Editor: Wei Huang

Received: 15 May 2024
Revised: 23 June 2024
Accepted: 24 June 2024
Published: 27 June 2024

Copyright: © 2024 by the authors. Licensee MDPI, Basel, Switzerland. This article is an open access article distributed under the terms and conditions of the Creative Commons Attribution (CC BY) license (https://creativecommons.org/licenses/by/4.0/).

1. Introduction

Hybrid rocket motor technology has advanced over the past decades, mainly trough ground research [1–3] but also flight testing [4], and it is now recognized as a potential alternative to the standard liquid and solid ones for multiple aerospace applications, for example sounding rockets [5], small launch vehicles [6,7] and suborbital space tourism [8].

Safety, reliability, architecture simplicity, throttleability [9–11] and re-ignition capability are the main advantages compared with the more conventional rocket motor technologies [12,13]. Moreover, the possibility of using green propellants (e.g., high-test peroxide, HTP) makes hybrid rockets an eco-friendly option compared with solid rocket motors and classical storable toxic liquids, increasing their attractiveness [14,15].

As a result of these advantages, hybrid rocket engines are expected to be increasingly adopted in the future. Furthermore, recent research addressed the main drawbacks (i.e., low fuel regression rate and low combustion efficiency) typical of the use of hybrid motors, and different effective solutions have been developed to improve performance to acceptable levels [16,17], at least for some applications.

For instance, the use of paraffin-based fuels has been proposed to considerably increase the regression rate values [18]. These types of fuels, called liquefying fuels, melt on the surface, and form a thin liquid layer where droplets are detached and entrained by the oxidizer gas flux, as described by the theory [19–21] and confirmed by experiments [22]. This added mass transfer mechanism leads to a higher regression rate [23] compared with classical diffusion-limited fuels [24–26] (e.g., hydroxyl-terminated polybutadiene, HTPB, or high-density polyethylene, HDPE). Additionally, recent studies examined the effects of additives to paraffin-based fuels, and the findings demonstrate the possibility of increasing the fuel thermo-mechanical properties (tensile strength increase over 40%) and tailor the fuel regression rate level (reductions up to over 50%) [27–29].

Devices such as post chambers (PC) [30], mixers and diaphragms [31–33] have been studied to enhance the mixing of the reactants by increasing the turbulence level in the combustion chamber, thus improving the combustion efficiency (above 90%).

One of the most effective means to improve both the regression rate and combustion efficiency is through vortex injection [34,35]. This type of injection forces the oxidizer flux to enter the combustion chamber with both tangential and axial velocity components, hence generating unique helical streamlines through the grain port. The vortex oxidizer injection can be placed at the head-end of the motor [36] or at the aft-end [37]. The resulting flow field increases the convective heat flux and the turbulence magnitude inside the combustion chamber. Thus, much higher values of the regression rate (several times' increase) and efficiency (above 90%) can be achieved [38–40].

The vortex intensity inside the chamber is quantified by the swirl number (SN). In each cross-section, the SN is defined as the ratio between the axial flux of the swirl momentum and the axial flux of the axial momentum [41].

$$SN = \frac{\int \rho v_z v_\theta r dA}{R_{max} \int \rho v_z^2 dA} \quad (1)$$

Since both the fuel regression rate and the combustion efficiency are related to the vortex intensity inside the combustion chamber, these variables are, likewise, linked to the SN parameter. Hence, vortex injection provides an additional advantage: the possibility of tailoring the fuel regression rate by adjusting the SN inside the grain port.

Regression rate tailoring is of particular importance as it permits varying the fuel radial ablation velocity, and thus the optimization of the combustion chamber design. Generally, the design objective is to maximize the volume loading (defined as the fuel volume divided by the chamber envelope volume), avoiding solutions that lead to a fuel-grain-length-to-diameter ratio (L/D) too low or too high [42–44], which negatively affects packaging and inert mass.

Regression rate tailoring has been investigated by using computational fluid dynamics (CFD) tools and by performing experimental tests [45], showing the possibility of changing grain consumption by over 50% by varying the injection swirl number while keeping high combustion efficiencies.

The most advanced hybrid rocket simulations are able to estimate the regression rate directly from the internal flowfield through mass, species and heat balances at the fuel surface, both for classical fuels [46,47] and also the more complex liquefying fuels [48–50]. Swirl injection has been also simulated numerically [51], confirming its peculiar flowfield and characteristics. CFD simulations are an effective tool to rapidly analyze multiple scenarios, providing detailed comparisons of the results. However, their reliability is highly dependent on the associated validation tests [52], which limit results generalization to

different parameters, propellants and/or configurations. Thus, experimental tests are still a necessary parallel choice, although more time consuming and expensive.

The experimental variation of the SN is enabled by the geometrical swirl number (SN_g). The SN_g is defined as the reference swirl number at the injection, and it depends only on the geometrical characteristics of the swirl injector plate. It is calculated using the following formula [53]:

$$SN_g = \frac{R_{inj}(R_{inj} - R_h)}{NR_h^2} \quad (2)$$

The SN_g is a useful parameter to perform the regression rate tailoring in vortex hybrid motors as it permits an easy and direct test results comparison just considering the injector plates' geometry and requires no difficult and intricate measurements of the internal flow field velocity components. In addition, previous works proved the existence of an approximately linear-like relation between the geometrical swirl number and the surface regression rate [45].

This work is part of the PHAEDRA (Paraffinic Hybrid Advanced Engine Demonstrator for Rocket Application) project coordinated by the Italian Space Agency [54]. The project aim is to develop a hybrid motor demonstrator for upper stage as reference application in order to investigate and exploit hybrid rocket engine (HRE) re-ignition capabilities, thus bringing hybrid motor technology to a large scale [55]. This paper focuses on the experimental investigation performed on a hybrid lab-scale motor to obtain the desired values of the regression rate and performance. These parameters were identified by the prime contractor Avio during the preliminary analysis phase.

The study reported hereafter investigates the regression rate obtained coupling different swirl injectors with different fuel types. The experimental setup consists in a lab-scale HTP hybrid rocket motor with a single-port grain. Two different fuels blend formulations based on paraffin (named as F8 and F5) and a third HDPE classical plastic fuel are tested; one of the former (F8) is coupled with a SN_g greater than 2, while the latter (F5 and the HDPE) are coupled with low swirl numbers (between 0.5 and 1.0). The two paraffin blend fuels were provided by Politecnico di Milano, a partner of the project, and they were developed in previous phases of PHAEDRA.

The results retrieved from the test campaign are reported in the following chapters. This study shows the great potential of having two variables (i.e., fuel formulation and SN_g) to tailor the fuel regression rate and optimize the combustion chamber design. Eventually, high values of combustion efficiency were obtained, even with the use of a lower SN_g, compared with the ones found in previous literature.

2. Materials and Methods

2.1. Motor Design and Configurations

The lab-scale hybrid motor used during the test campaigns is composed of four main components: (1) a catalyst bed containing catalytic material, where the HTP is decomposed producing high-temperature O_2 and H_2O vapor; (2) a swirl injector imposing a rotation to the oxidizer flow along the motor axis; (3) a combustion chamber where the reactions between the oxidizer and the fuel grain (i.e., HDPE and paraffin-based fuels) occur; and (4) a nozzle holder encasing the graphite nozzle insert.

The catalyst bed and the combustion chamber metal case are connected by a clamp-type joint with a graphite braid providing gas sealing. The combustion chamber structural case is made of steel and consists of two flanges and a hollow cylinder between them. A set of eight M16 rods close the flanges against the cylinder.

The vortex injection plate is placed inside the inlet flange of the motor case. The combustion chamber parts (e.g., fuel grain, post chamber and thermal protection, TP) are bonded together using a silicone filler. These assembled consumables form the so-called motor cartridge, which can be easily integrated and removed from the cylindrical metal case. The nozzle holder is screwed to the outlet flange with a silicon O-ring, ensuring the sealing from the combustion gases.

The aft part of the catalyst assembly is connected to the fluidic line once the motor is placed on the test bench (Figure 1).

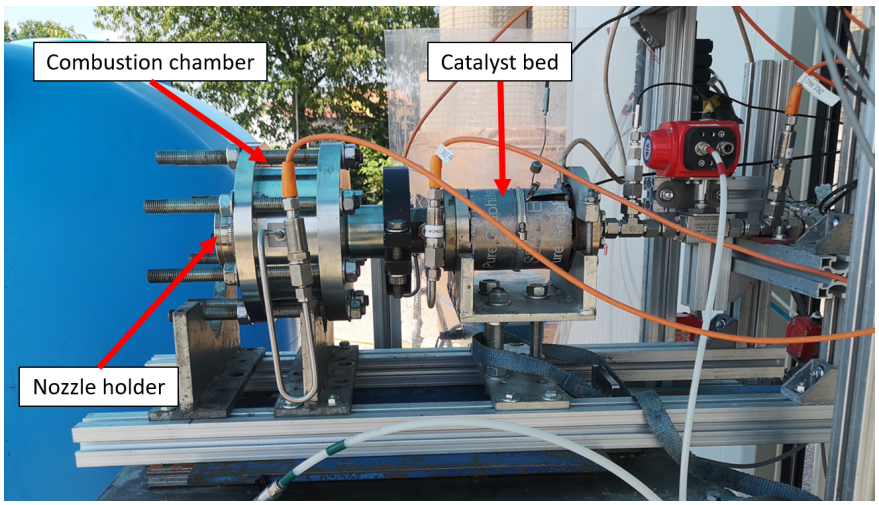

Figure 1. The lab-scale hybrid motor assembled and installed on the test bench.

The catalyst bed, nozzle and metal flanges were kept unchanged across the campaign, while the swirl number and the combustion chamber configuration varied. In the combustion chamber, this was done either by changing the fuel type (i.e., F5, F8 and HDPE), or the fuel length and initial port diameter, or by adding a post-combustion chamber. These changes were necessary to ensure an optimal oxidizer-to-fuel (O/F) ratio and combustion efficiency, which could decrease when using a low SN_g.

The oxidizer injection SN_g was altered by changing the vortex injector cup. This metal part is installed on the flange between the catalyst bed and the combustion chamber. For an axial oxidizer injection, a metal ring is assembled in place of the swirl injector.

Figure 2 shows the vortex injector position and the motor configurations with and without the addition of the post chamber and with different grain initial port diameters.

2.1.1. Vortex Injector

The vortex injector controls the swirl flowfield intensity inside the combustion chamber. Thus, the design of this component is strictly related to the regression rate achieved.

The design of the injector consists in sizing the geometric dimension and the number of the tangential holes, and the cup internal radius, as indicated in Figure 3.

The fuel regression rate could be adjusted during the motor design stage based on the vortex intensity imposed by the injector geometrical characteristics. Using Formula (2), it is possible to obtain the desired SN_g, where R_{inj} is the injector internal radius, R_h is the hole radius and N is the holes number.

These parameters make the vortex injector geometry a powerful degree of freedom for the regression rate tailoring, as already proven in [45].

There are 6 injectors used in this experimental campaign; they are made of 316L stainless steel and their geometrical swirl numbers are 0.50, 0.75, 1.00, 2.00, 2.50, 3.33.

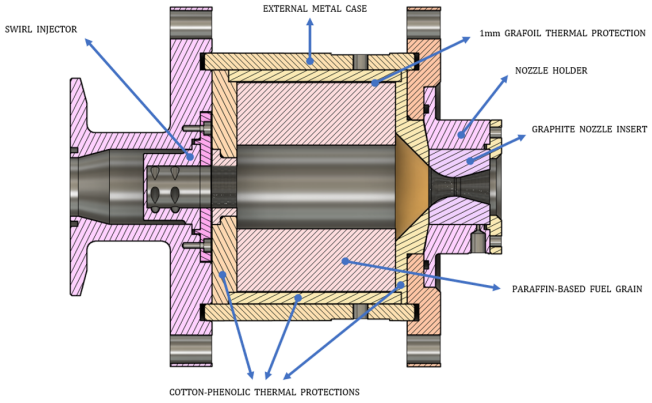

(**a**) Wider fuel port.

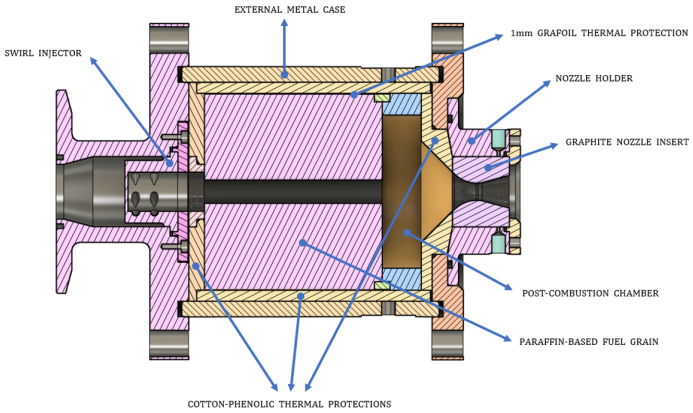

(**b**) Post-combustion chamber.

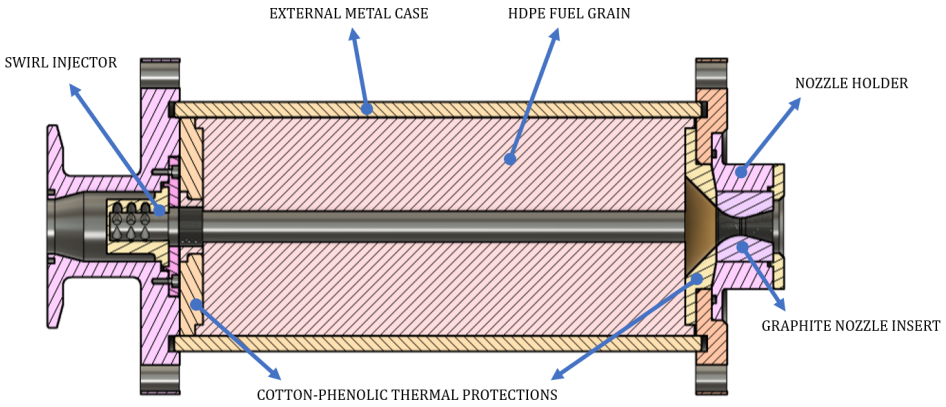

(**c**) HPDE fuel grain.

Figure 2. The different internal motor configurations used during the experimental test campaign. (**a**) Configuration with a paraffin-based fuel grain and a wider grain port. (**b**) Configuration with a paraffin-based fuel grain and the combustion post chamber. (**c**) HDPE fuel motor configuration. No fuel jacket is needed to accommodate the grain.

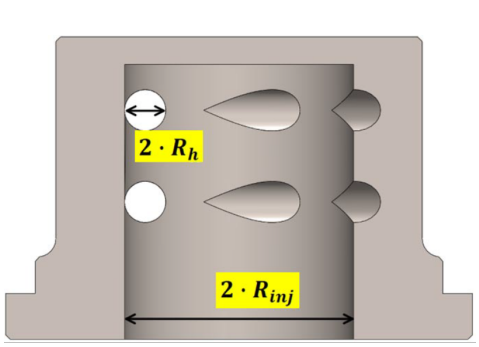

(**a**)

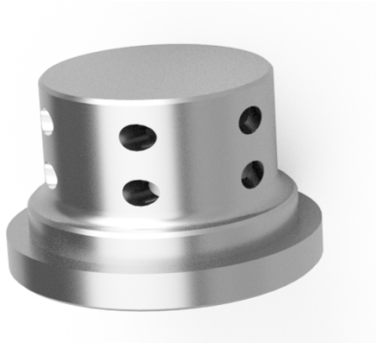

(**b**)

Figure 3. The vortex injector. (**a**) The geometrical parameters characterizing the vortex injector SN_g. Reprinted with permission [45]. (**b**) A three-dimensional injector view.

2.1.2. Combustion Chamber

The combustion chamber includes the injection insert, the fuel grain, the post chamber and the thermal protections. An exploded view of these consumables is displayed in Figure 4.

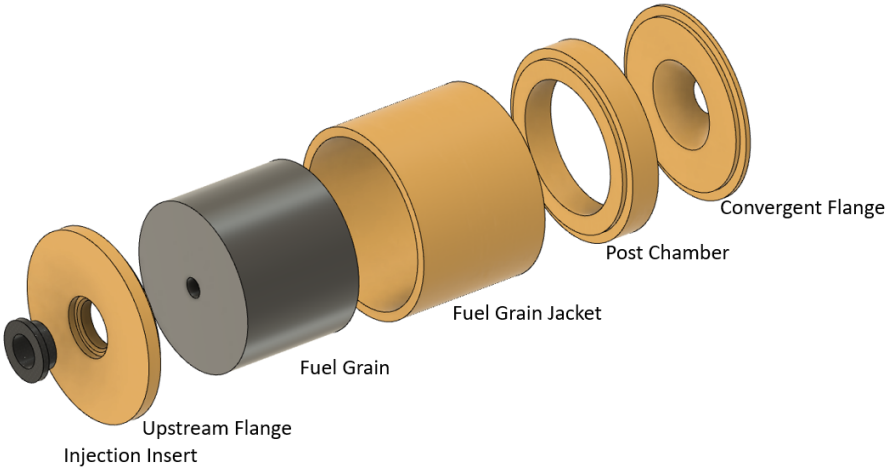

Figure 4. The exploded view of the motor cartridge with the consumables named.

All the thermal protections components (ochre-coloured) are made of cotton phenolic. The convergent and the upstream flanges protect the motor case metal flanges from the high temperature of the combustion gases. Moreover, the upstream flange holds a graphite injection ring. The insert shields the internal hole of the upstream flange, which otherwise would be excessively eroded by the swirled high oxidizing flow.

The cotton phenolic erosion rate is fairly low compared with the fuel grain consumption. In addition, the surfaces exposed to the flame are minor, and thus the contribution to the fuel mass burned is lower than 10%. Moreover, the TP characteristic velocity is only slightly lower than that of the fuel.

The fuel grain jacket is not present in motor configurations using the HDPE as the fuel grain material. The tests performed with HDPE do not entirely use the fuel grain. The residual thickness acts as a jacket, preventing the heating of the cylindrical metal case.

The post-combustion chamber is used in some tests with paraffin-based fuels. Generally, this element is not needed in a vortex hybrid motor, since a high combustion efficiency is already achieved thanks to the swirled flowfield. Nonetheless, in our investigation, it has been useful for increasing the combustion gases' residence time inside the chamber in particularly compact motor configurations. The post chamber is a hollow cylinder with an internal diameter of 100 mm, while the cylindrical length (L_{PC}) varies. The L_{PC}/L_{grain} ratio is used to determines the post chamber length. The tested values of this parameter are 23%, 30% and 42%.

A simple side-burning grain with a circular port, whose dimension is constant along the motor axis, serves as the fuel. Then, to fully define its shape, three measurements are required: the length, the external diameter and the initial port diameter. Every paraffin-based fuel grain has an exterior diameter of 125 mm, while the HDPE fuels measure 140 mm, due to the absence of the cotton phenolic jacket. For each of the examined grains, a different combination of the other two geometrical factors is used. Regression rate coefficients from earlier experimental data or from the experimental data retrieved in the actual test campaign are used to define both the internal diameter and the length.

The initial port diameter ranges from a minimum of 15 mm to a maximum of 65 mm. The minimum value allows to not exceed the threshold of 950 kg/m^{2}s for the oxidizer mass flux (G_{ox}). The maximum allowable value depends on the estimated grain thickness burned during the test. In tests where the port diameter is increased, the objective is to lower the average G_{ox} value over the burning time, i.e., to reduce the combustion gases' velocity inside the chamber, thus increasing their residence time. The length of the grain is adjusted from test to test to obtain the desired oxidizer-to-fuel ratio (O/F). In the case of paraffin or HDPE hybrid engines, the optimal O/F value is between 6.5 and 7.5.

The influence of the fuel grain material is the other important parameter investigated in this study. The possibility of using distinct fuel types with calibrated amounts of additives in the fuel mixtures allows the achievement of different regression rate levels. Moreover, coupling this feature with the opportunity to change the SN_g in hybrid vortex motors gives two degrees of freedom to extend the regression rate tailoring, and hence to optimize more easily the hybrid rocket motor design.

A total of three fuel types are investigated in this research. Two of them are paraffin-based fuel mixtures with additives, and they are named F5 and F8. These blend formulations were chosen during the previous steps of the PHAEDRA project and they are produced by the partner Politecnico di Milano. The third fuel type is made of conventional HDPE.

To be representative of the large-scale application, the corresponding lab-scale motor requirements are:

- Maximum expected operating pressure (MEOP) of the combustion chamber (P_{cc}) in the range of 30–35 bar;
- Burning time of 17 s;
- Combustion efficiency (η_{c^*}) greater than 95%.

The pressure inside the combustion chamber can be estimated by the following formula:

$$P_{cc} = \frac{\dot{m}_{ox}(1 + \frac{1}{O/F})c^*}{A_t} \tag{3}$$

where $\dot{m}_{ox}$ is the oxidizer mass flow, c^* is the characteristic velocity of combustion gases and A_t is the nozzle throat area.

The theoretical vacuum performance of 95% HTP with paraffin wax at O/F = 7.5, an expansion ratio of 60 and 30 bar chamber pressure include a specific impulse of 327 s, a c^* of 1632 m/s, an average density of 1314 kg/m^3 and an impulse density of 4200 kNs/m^3.

The target $\dot{m}_{ox}$ value is set to 0.156 g/s and it remains unchanged for the entire test campaign. Then, the NASA thermo-chemical code Chemical Equilibrium with Applications (CEA) is used to predict the c^* of the chemical species that is produced during the combustion of the hydrogen peroxide with the corresponding fuel inside the combustion chamber.

The model implemented to simulate the fuel grain port diameter variation during the burning time, to estimate the O/F, is based on the Marxman law:

$$\dot{r} = aG_{ox}^n \tag{4}$$

where the constant a is determined in the post-processing analysis, and the second constant n, which is related to the fuel/injection type, is assumed to be equal to 0.5. This assumption has been already demonstrated to be acceptable for paraffin and HDPE fuels in the literature [42,56] and corroborated in a similar experimental setup tested in the internal facility.

2.1.3. Nozzle

The nozzle insert is made of graphite, and it is placed inside the nozzle holder (Figure 5). The throat diameter is fixed, specifically equal to 11.0 mm. With an exit pressure of 1 atm, the exit diameter of 21.0 mm is designed to achieve nearly perfect adaptation. The calculated expansion ratio is 3.6.

2.2. Experimental Setup

The experimental set-up is composed of the fluidic line, which regulates the oxidizer mass flow, the mobile test bench, where the lab-scale hybrid motor is fixed, and the measurement system, necessary to monitor and collect the sensors data during the testing activity. In the following, a more detailed description of each component is given.

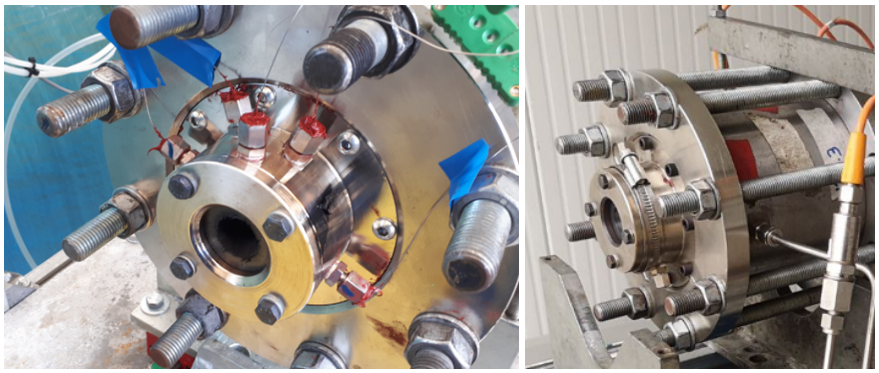

Figure 5. The graphite nozzle insert placed within the nozzle holder.

2.2.1. Fluidic Line

The pressurization system is the first component of the fluidic line and is a pressure-fed system providing the amount of gas needed to drive the oxidizer from the tank to the combustion chamber. The combustion chamber has a pressure ranging between 25 and 30 bar. Thus, a pressure higher than 30 bar is required to impose a forced motion of the oxidizer from the tank to the combustion chamber. Particularly, the pressurization system is composed of high-pressure (i.e., 100–200 bar) nitrogen (N_2) cylinders, a pressure-regulating system, in-line filter, control valves, and rigid and flexible connections. Thanks to the manual spring-loaded regulator, different pressures can be used inside the pressurization line. The pressure regulator is linked to a $1/2''$ pipework with various manual and pneumatic valves.

Then, the fluidic line continues with the propellant feeding line composed of the hydrogen peroxide tank, the cavitating venturi (CV), and a series of tubes and ball valves in AISI 316L stainless steel. The oxidizer tank has a volume of 20 L and can withstand a pressure of 120 atm. The upper shell is equipped with a rupture disk that breaks before the pressure can reach the tank maximum operative pressure. This is a safety system in case of HTP unexpected decomposition taking place in the propellant feeding line.

The CV is the element used to control the oxidizer mass flow. In a CV, the operating fluid reaches the saturation pressure at the throat section, and thereby the flow is limited by the onset and growth of vapor pockets. The choice of the CV throat area depends on the oxidizer tank pressure and on the desired oxidizer mass flow, related to Equation (5) defined in [57]:

$$\dot{m}_{ox} = A_{th} c_d \sqrt{2\rho_{HTP}(P_{0,up} - P_{sat})} \tag{5}$$

2.2.2. Mobile Test Bench

The bench is made up of a tubular steel structure that can be forked with a forklift, allowing its movement from the workshop to the testing area. At the base of the bench there are perforated brackets to fix the structure to the test container floor by means of dowels, to avoid any kind of tipping. Above the structure, a steel plate acts as the main plane. On this plate, a pair of parallel linear guides are fixed. Over these guides, a further plate is capable of sliding in the axial direction by means of linear rail bearings.

The motor supports are connected to the sliding plate, and their position can be adapted depending on the motor configuration length. The plate is placed at one end in touch with a load cell to measure the thrust during the test. The cell is placed on a structure that acts as a thrust bearing. To prevent the plate from slipping off, a blocking screw is positioned on the opposite side of the cell. Figure 6 shows the lab-scale hybrid motor mounted on the mobile test bench.

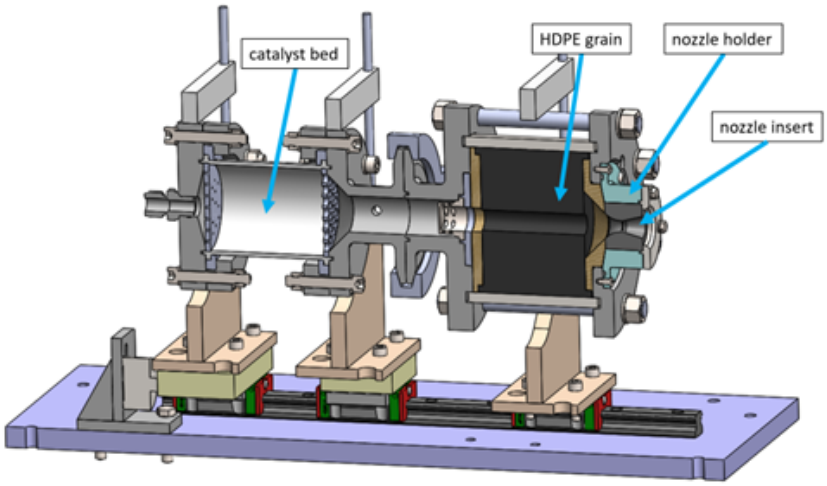

Figure 6. Cross section of the lab-scale hybrid motor.

2.2.3. Measurement System

The core of the measurement system is a data logger. The logging system collects the sensor signal with an acquisition frequency of 1 kHz. To monitor pressures and temperatures during the tests, several gauges and thermocouples (type K) are installed along the fluidic line and on the hybrid motor. The quantities collected are upstream and downstream N_2 pressure regulator (PR) pressures, oxidizer tank pressure and temperature, CV upstream pressure, catalyst bed inlet pressure and temperature, catalyst bed outlet pressure and temperature, and combustion chamber pressure. Due to their importance for the motor performance analysis, the combustion chamber pressure sensors are redundant. The oxidizer mass flow to the combustion chamber can be measured directly thanks to a Coriolis mass flow meter, which is positioned near the outlet of the oxidizer tank. The motor thrust is measured by means of a load-cell. The sensor list is reported in Table 1.

Table 1. List of the gauges used to monitor the pressures, temperatures, oxidizer mass flow and motor thrust. These data are collected to be analyzed and post processed after the experimental test.

Position	Measured Variable	Range	Accuracy
Upstream PR	Pressure	0–250 bar	±1.25 bar
Downstream PR	Pressure	0–160 bar	±0.8 bar
Oxidizer tank	Pressure	0–250 bar	±1.25 bar
Upstream CV	Pressure	0–100 bar	±0.5 bar
Inlet catalyst bed	Pressure	0–100 bar	±0.5 bar
Outlet catalyst bed	Pressure	0–60 bar	±0.3 bar
Combustion chamber	Pressure	0–100 bar	±0.5 bar
Combustion chamber	Pressure	0–60 bar	±0.3 bar
Oxidizer tank	Temperature	0–1100 °C	±2.2 °C or ±0.75% [1]
Inlet catalyst bed	Temperature	0–1100 °C	±2.2 °C or ±0.75% [1]
Outlet catalyst bed	Temperature	0–1100 °C	±2.2 °C or ±0.75% [1]
Oxidizer mass flow	Mass flow	0–5 kg/s	±0.75%
Motor thrust	Thrust	0–1000 kg	≤0.03%

[1] Thermocouple true accuracy is the lower of the two values, according to the measurement.

The measurement system also includes the instruments necessary to measure the physical dimensions of the motor's consumables. A scale, with an uncertainty of 1 g, is used to weigh each component of the combustion chamber both before and after the test. Additionally, a dimensional control of the components is performed with a vernier caliper (uncertainty of 0.05 mm) to ensure that the dimensions meet the tolerances specified in the technical drawings.

2.3. Test Matrix

To better understand the fluidodynamic behavior at low values of the SN_g, a preliminary numerical analysis was carried out prior to define the experimental test matrix. CFD numerical simulations were performed by Sapienza University of Rome, a PHAEDRA project partner, to examine the combustion chamber internal flowfield with low swirl numbers, two fuel formulations (including the F5) and various post chamber lengths (Figures 7 and 8 from [50]). The results were encouraging for the proceeding of the work. The length of the grains in the initial tests and the length of the post chambers were two examples of the parameters that were defined using the results.

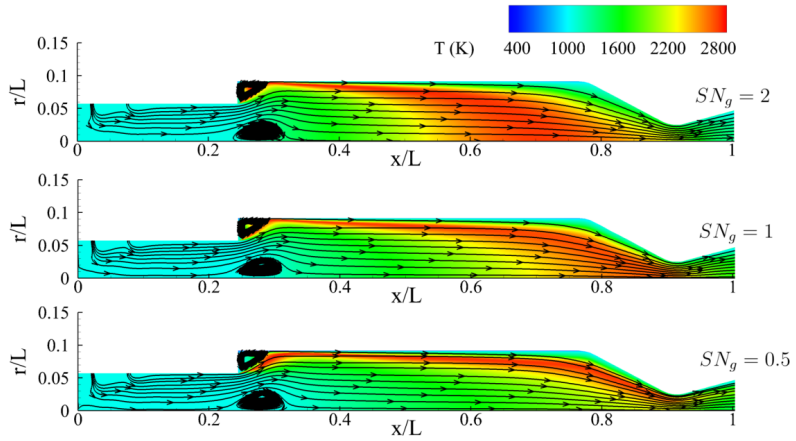

Figure 7. Temperature flowfield with varying swirl intensities (F2 formulation). Adapted, with permission, from [50].

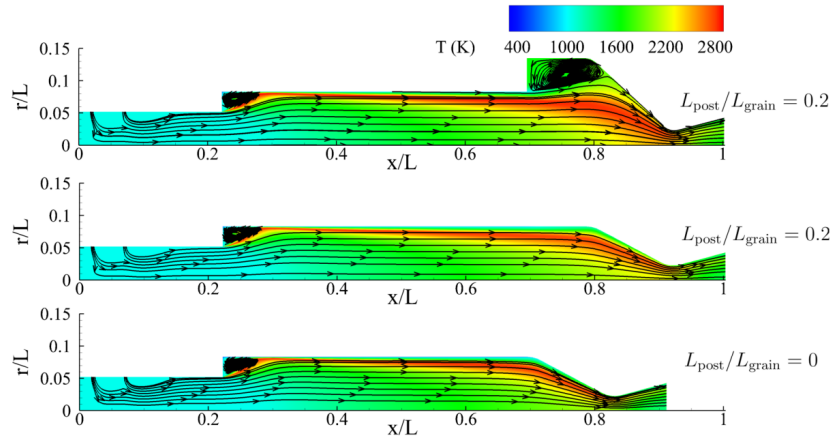

Figure 8. Temperature flowfield with varying post chamber configurations. Adapted, with permission, from [50].

The F8 blend was the first fuel type tested. This formulation was chosen as the reference paraffin-based fuel for the PHAEDRA project. This paraffin combines a relatively high regression rate and good mechanical properties. Thus, it was decided to test F8 paraffin throughout an extensive spectrum of the SN_g. The geometrical swirl number of the tests extended from zero, or axial flow, up to the value of 3.33. During the course of the investigation, the grain length was adjusted to be closer to the ideal O/F value based on the findings of earlier trials.

A total of ten fire tests were executed. Only one F8 paraffin grain was tested with a different initial port diameter (F8_008), while two other configurations included the post chamber (F8_001–F8_002). Most of the tests performed had durations of 10 s and 15 s, which allowed us to perform regression assessments and performance calculations for two distinct average oxidizer mass flux values. Since the initial test main goal was to confirm that the fuel would ignite, it was scheduled for a shorter period.

The second phase of the test campaign focused on vortex injectors with low swirl number values. Along with evaluating the regression rate, the goal was to confirm how efficiency changes when the vortex intensity inside the chamber decreases. It has been possible to compare the collected data with those found in the literature thanks to the utilization of a standard polyethylene fuel. Furthermore, HDPE is less susceptible to post-burn effects (such as grain port surface melting and thermal deformations), which makes it possible to quantify and observe the fuel consumption rate more accurately.

A total of six tests were performed: each of the three vortex injectors, with the SN_g equal to 0.50, 0.75 and 1.00, were tested twice, varying the oxidizer mass flow running time, 15 s and 20 s, respectively. Throughout the experiments, the fuel initial port diameter, which was set at 20 mm, did not change. Otherwise, to reach the desired O/F value, the grain length was varied.

The final leg of testing was carried out using formulation F5. This paraffin blend has a composition different from F8, and produces a comparatively lower regression rate. In addition to investigating a different blend, this campaign completed the results gained in prior tests, and, indeed, it examined the low swirl numbers coupled to a paraffin-based fuel. At this point, it was also possible to focus on the variation in combustion efficiency as the chamber volume changed.

There were nine tests run, three of which (F5_002, F5_003 and F5_004) had a SN_g equal to 1, and the remaining six had a value of 0.75. The grain length of 95.1 mm varied only in the first and last sample of this series (F5_001 and F5_009). The F5_003 test was the only one with a varied experimental duration with respect to 15 s; it fired indeed for 20 s. The post chamber was added to F5_005 and to the last three tests. Initial fuel port diameters of 15 mm, 50 mm and 65 mm were examined.

In Table 2, the entire test matrix is displayed together with the key data from each test individually.

Table 2. List of salient features of the firing tests performed for this investigation.

Test	Fuel Type	SN_g [-]	Test Duration [s]	PC-to-Grain-Length Ratio [-]
F8_001	F8 paraffin	3.33	5.5	22.0%
F8_002	F8 paraffin	2.00	10.5	22.0%
F8_003	F8 paraffin	0.00	17.0	-
F8_004	F8 paraffin	2.00	17.0	-
F8_005	F8 paraffin	2.00	10.0	-
F8_006	F8 paraffin	2.00	10.0	-
F8_007	F8 paraffin	2.00	17.0	-
F8_008	F8 paraffin	2.00	10.0	-
F8_009	F8 paraffin	2.00	10.0	-
PE_001	Polyethylene	1.00	20.0	-
PE_002	Polyethylene	1.00	20.0	-
PE_003	Polyethylene	0.50	20.0	-
PE_004	Polyethylene	0.50	15.0	-
PE_005	Polyethylene	0.75	15.0	-
PE_006	Polyethylene	0.75	20.0	-
F5_001	F5 paraffin	0.75	15.0	-
F5_002	F5 paraffin	1.00	15.0	-
F5_003	F5 paraffin	1.00	20.0	-
F5_004	F5 paraffin	1.00	15.0	-
F5_005	F5 paraffin	0.75	15.0	23.0%
F5_006	F5 paraffin	0.75	15.0	-
F5_007	F5 paraffin	0.75	15.0	23.0%
F5_008	F5 paraffin	0.75	15.0	42.0%
F5_009	F5 paraffin	0.75	15.0	30.0%

2.4. Data Post Processing

At the end of each test session, the regression rate law a value, and the combustion efficiency (η_{c^*}) were estimated. a is the first constant in the Marxman law Equation (4) that models the grain port regression. This number is calculated by assessing the radial thickness of the fuel consumed throughout the burning period. η_{c^*} is defined by:

$$\eta_{c^*} = \frac{c^*_{exp}}{c^*_{th}} \tag{6}$$

where c^*_{th} is retrieved from the NASA CEA code and c^*_{exp} is computed using the following equation:

$$c^* = \frac{P_{cc} A_t}{\dot{m}_{ox}(1 + \frac{1}{O/F})} \tag{7}$$

The experimental c^* value is calculated using both the data collected during the tests and the internal component measurements.

To do so, the lab-scale hybrid motor is disassembled at the end of each test to assess the engine consumables, namely, fuel grain, thermal protections and nozzle insert. Figure 9 illustrates the parts after the disassembly. Then, the mass of each component is evaluated to estimate the amount of material involved in the combustion. The sum of the burned mass contributions is called the fuel mass (m_f).

Figure 9. Disassembled parts of the lab-scale hybrid motor after the firing test.

Also, at the conclusion of each test, both the fuel grain and the nozzle insert are measured by means of the vernier caliper. By measuring the throat diameter of the graphite insert, the erosion value of the throat area at the end of the test may be computed (A_{th-fin}).

The grain web thickness burnt during the test is computed using the measurement of the fuel final port diameter ($\Phi_{port-fin}$). However, the degradation of the grain port is not constant along the longitudinal axis. Furthermore, also the rear face is consumed, especially in the cases where the post chamber is present. So, along the grain port, the diameter is measured in three different points; moreover, in the case of rear face consumption, its diameter and depth are taken. It is important to emphasize that the average of the diameters along the grain port and the quantity of fuel burned less the mass calculated from the face consumption are utilized during post processing to obtain the regression rate constant a. Consequently, rear face consumption is seen as a continuous fuel injection during the burn that is independent of port diameter erosion.

Figure 10 depicts the fuel grain measurements collected.

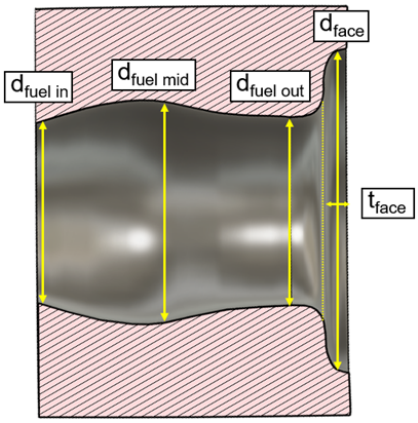

Figure 10. The fuel grain geometrical measurements. Grain port non-uniform longitudinal regression and rear face consumption.

Once the sensor data have been collected, the estimation of the ignition and burning time can be computed by analyzing the combustion chamber pressure plot.

The ignition time is considered as the time spanned between the first change in the outlet catalyst bed pressure plot (after the *V_test* opening electric input) and the achievement of 90% of the combustion chamber pressure. The burning time (t_b) spans from the end of the ignition time and the *V_test* closing electric input. These two time intervals are highlighted in Figure 11. Average engine performance parameters are evaluated referring to the burning time just defined.

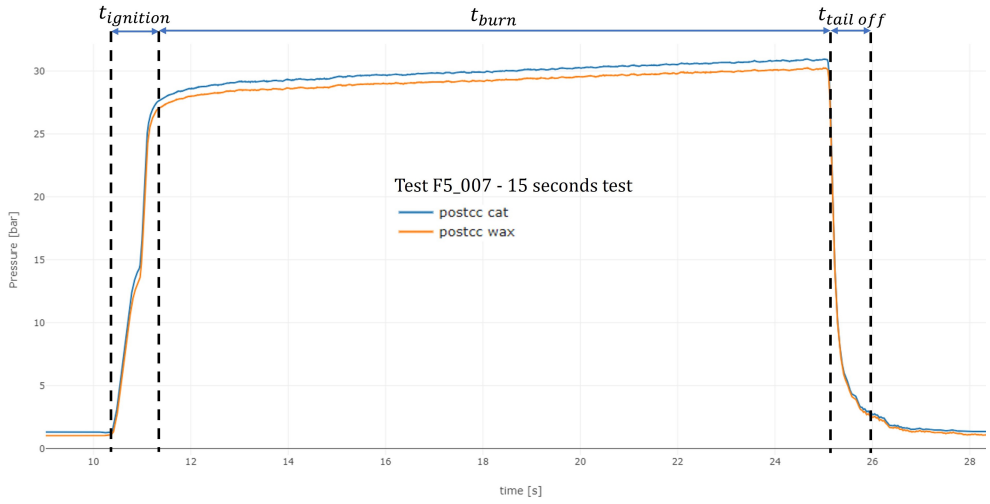

Figure 11. Ignition and burning times identified on the pressure plot of a F5 15-second test. The logged pressure signal has been filtered.

Once the burning time is retrieved, it is possible to compute the average O/F as:

$$O/F = \frac{\dot{m}_{ox}}{\dot{m}_{fuel}} \tag{8}$$

where $\dot{m}_{fuel} = m_{fuel}/t_b$.

An iterative approach is used to perform the regression rate analysis and simulate the Marxman law over the burning time span. The initial conditions are (1) the initial G_{ox}, calculated from the measured $\Phi_{port-in}$ and the collected oxidizer mass flow; and (2) the first guess value of a. Then, the code will calculate the grain port regression during the burning

time and the fuel mass burned. At every iteration, the a constant of the regression rate is updated until it converges to a final value that matches the fuel grain consumption gathered from the weighted burned mass (a_{mass}) or the final port average diameter measures (a_{phi}). The loop is schematized in Figure 12.

Motor performance is computed by another iterative algorithm. The burning time is divided into 100 points, and the equations for calculating the experimental and theoretical c* are employed at each point. At each step the inputs are (1) oxidizer mass flow and combustion chamber pressure from the data acquisition; (2) O/F, nozzle throat area and grain port diameter from the measurements; and (3) c^*_{th} from CEA routine. The instantaneous throat diameter is calculated considering a linear erosion during the burn, while the port diameter comes from the previous calculations. As a code result, there is a combustion efficiency vector for the entire fire test duration. Thus, the average combustion efficiency of the test analyzed is the resultant vector average (see Figure 12). This average is strictly correct only in the absence of mixture ratio shift during the burn, which is justified by a constant oxidizer flow and the assumption of an n exponent equal to 0.5.

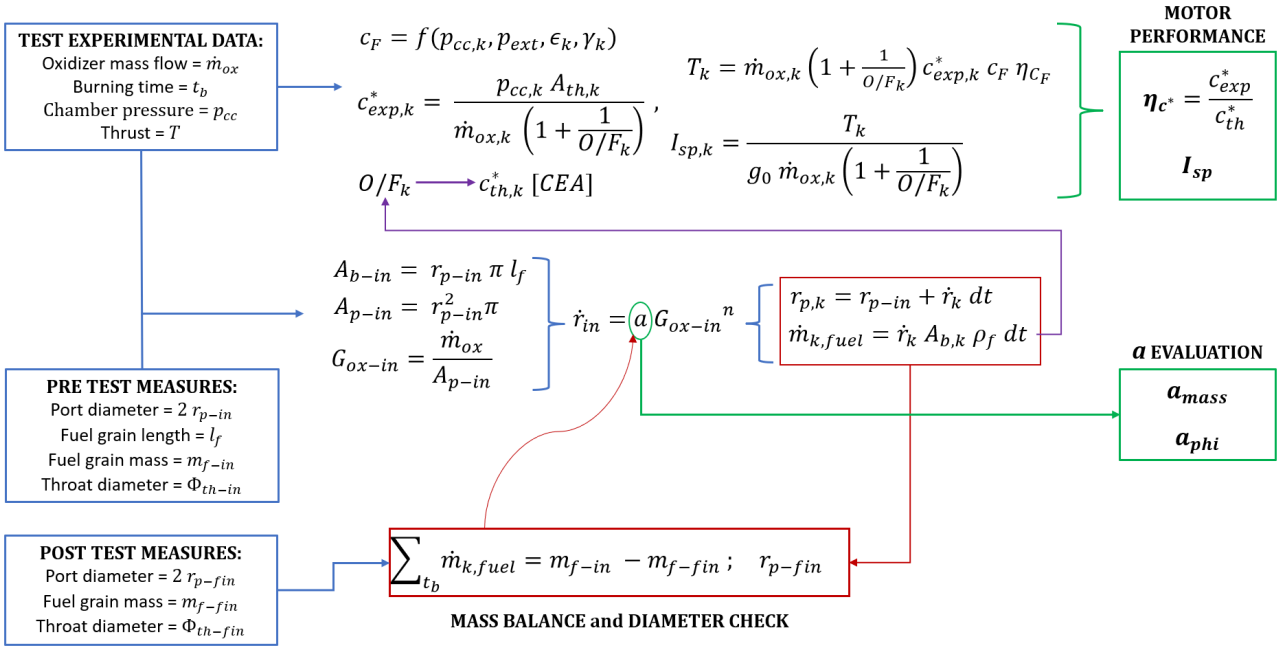

Figure 12. A visual summary of the recursive methods, gathered sensor data and geometrical measurements implemented in the output computation scheme. The blue boxes represent the input data. The iterative loop that determines the a constant and models the fuel regression rate is indicated by red boxes and arrows. In comparison, the second method, which iterates over the burning time vector, is represented in the central portion of the upper part and denoted by k subscript. The output variables of the calculation scheme are in green boxes.

3. Results

This section outlines the experimental campaign results for the tested SN_g values and the three fuel types. In each subsection is reported:

- the results of the pertinent test campaign calculated during the post-processing analysis;
- the experimental curves of the constant a plotted against the SN_g.

Concerning the constant a_{exp}, its value is equivalent to the a_{mass} computed in the regression rate modeling algorithm. The different longitudinal unevenness of the consumption between the experiments, which was strongly dependent on the fuel type, the grain length and the vortex injector geometry, prevented the possibility of identifying a consistent and reliable method to approximate a_{phi}. For this reason, this value has been excluded from the results. For each test, an average of the diameters measured in the post-burn analysis weighted on the grain length should be implemented in order to improve the a_{phi} estimation.

3.1. F8 Test Results

Using the F8 paraffin formulation, nine fires were executed in a wide range of SN_g values from 0 (axial) to 3.33. There were very few differences in the oxidizer mass flow between tests. A technical error in the oxidizer tank pressure regulator setting caused the mean value of test number F8_006 to unexpectedly increase to 163 g/s. It had no effect on the regression rate computation, though.

The regression rate in the first test (SN_g = 3.33) was extremely high. This fuel consumption caused the O/F ratio to decrease too much, which made the combustion unstable. As a result, the motor ignition took longer than usual. The zero SN_g (i.e., axial flow) test revealed the effect of the additives; in fact, the regression rate obtained is lower than the pure paraffin reference rate tested in the past (0.139 vs. 0.15). The post chamber was no longer used for the remaining SN_g tests since it generated pressure instabilities noticeable through pressure peaks on the combustion chamber sensor graph during the burn phase. For this swirl number of 2, the average value of a was 0.4.

The combustion efficiency with a high SN_g is acceptable (greater than 93%), but it is slightly lower than usual. The most plausible explanations are that, in certain tests (F8_001 and F8_002), the O/F ratio was significantly off from ideal (i.e., O/F approximate to 3) and, in other tests, the chamber volume was significantly lowered as a result of the grains' shorter length. The combustion efficiency of test F8_003 was low (lower than 90%), even with an optimal O/F, because no device was installed to increase the turbulence level inside the chamber.

A linear relationship can be reasonably assumed by plotting the values of the constant a and the related SN_g on a graph (Figure 13). Then, two least squares lines are drawn within its equations, with one of them having its intercept fixed to 0.139 (axial a value).

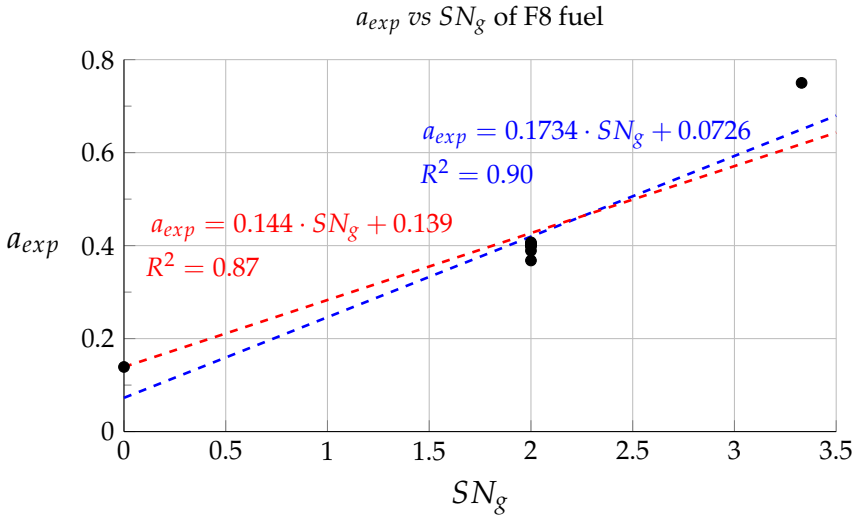

Figure 13. The values of the a_{exp} constant are plotted against the corresponding SN_g. The black dots correspond to the values obtained through experiments. The blue dashed line is the least squares line, and likewise the red dashed line, where the intercept is set to the value 0.139.

3.2. HDPE Test Results

The HDPE fuel was used in six experiments. The tests were performed using low swirl numbers, ranging from 0.50 to 1.00. These SN_g provide longer fuel grains than paraffin ones when combined with HDPE fuel; hence, with the same G_{ox}, the residence time of the combustion gases is significantly higher.

Indeed, the motor efficiency was greater than 96.6%, except for the first test, where it reached a value of 92.6%. This anomaly could perhaps be related to the fact that the value of the mixture ratio during combustion was less close to the optimal if compared with the other results (i.e., O/F equal to 5.5 versus values ranging between 6.0 and 6.5).

With the exception of the initial test, the oxidizer mass flow consistently measured around 156 g/s. A little particle that passed through the cavitating venturi throat is likely what caused the abrupt downturn and upturn in the mass flow meter curve of the PE_001 trial.

It is reasonable to presume the existence of a linear relationship by inserting the values of the constant a and the related SN_g on a graph. Next, a least squares line is sketched and its equation is given (Figure 14).

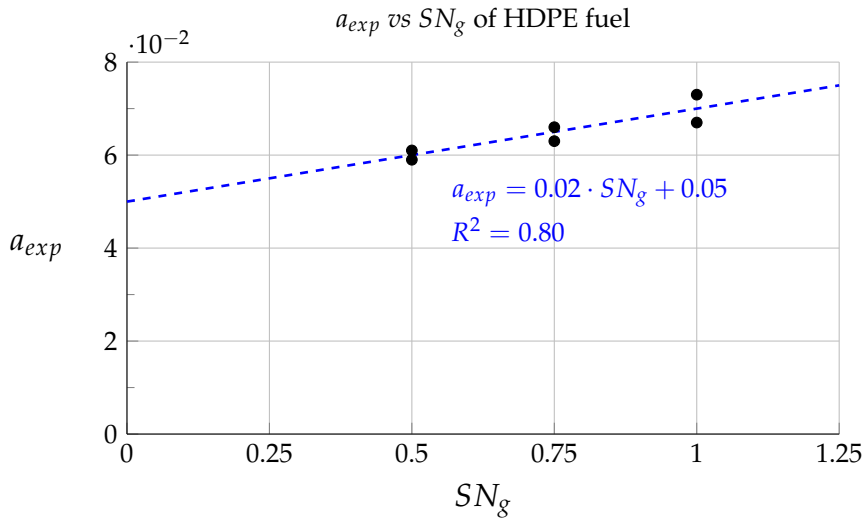

Figure 14. The values of the a_{exp} constant are plotted against the corresponding SN_g. The black dots correspond to the experimental points. The blue dashed line is the least squares line and the relation is reported in the graph.

3.3. F5 Test Results

Nine tests were conducted on the F5 paraffin fuel formulation. The vortex injectors SN_g used in this campaign were 0.75 and 1.00. The mass flow curves of the oxidizer exhibited no anomalies.

The combustion efficiency was above 90% but less than 95% in the majority of tests, although it exceeded this threshold in tests F5_004, F5_008, and F5_009.

The impact of the post chamber was examined in the concluding three tests of the campaign, for values of the L_{post}/L_{fuel} ratio of 23%, 42% and 30%, respectively. Efficiency increased, although not linearly, as the L_{post}/L_{fuel} factor increased. The regression rate stayed consistent with the other experiments at a swirl number of 0.75, even though the grain rear face remained more exposed during the burning time.

Test F5_004 yielded a very high efficiency (greater than 95%) even though it lacked the post chamber and operated with a very unfavorable O/F value. The employment of a higher swirl and a very low G_{ox} (i.e., a greater initial fuel port diameter), which raises the motor volume and the residence time, is what probably accounts for the efficiency gain. The positive impact of these variables is also evident in those tests where inserting the post camera or widening the grain port diameter resulted in a higher efficiency than the first three experiments.

4. Discussion

This work had several goals: (1) demonstrate that vortex injection can be used successfully with liquefying fuels; (2) investigate how low swirl numbers ($SN_g < 1$) affect hybrid motor performance; (3) exhibit the potential of playing with two design variables (fuel composition and swirl number) to perform regression rate tailoring; and (4) identify the optimal set of parameters to fulfill the PHAEDRA project requirements.

The first objective, the effective use of vortex injection together with liquefying fuels, has been confirmed. In fact, the first and third test campaigns have demonstrated:

- Rapid fuel ignition, with the burning time almost corresponding to the oxidizer valve opening time;
- Stable combustion for the majority of cases, with no anomalies from the graphs of the two pressure sensors in the motor.
- An approximate straight line correlation between swirl number and regression rate, proving the possibility of tailoring the grain geometry by selecting the proper fuel-SN_g combination.

This has been verified for two very different paraffin formulations and four different swirls numbers (i.e., 0.75, 1.00, 2.00, 3.33). It is important to underline that the relation between the regression rate and the swirl number can be approximated with a straight line that intersects the Y-axis with a positive bias, and therefore the behavior of the regression rate with the swirl number is sub-linear, i.e., doubling the swirl number provides a much lower increase in fuel consumption. Moreover, the real behavior of the regression rate with the swirl number should be more accurately approximated by a relation like $(1 + SN_g^2)^m$ [10], so the fits shown in this paper should be used with caution, particularly outside the ranges from which they were inferred.

For the high regressing F8 paraffin with a $SN_g > 2$, the regression rates achieved are up to 5 times higher than usual for paraffin, and even 15 times higher than classical fuels with axial injection. These impressive results could pave the way for the effective utilization of single port hybrid rocket motors at larger scales (rule of thumb > 100 kN) and/or shorter burning times than usually considered. Unfortunately, the lab scale involved in the tests is on the opposite spectrum of size with respect to these favorable cases, producing very short, stubby fuel grains ($L/D < 1$) and small combustion chamber volumes. The short residence time probably negatively affected the vaporization of the entrained droplets. The fact that the efficiency with vortex injection is already above 90% level at this small scale is a promising indication that very high levels should be possible to be achieved at the targeted larger scales where the residence time is longer and the grain geometry is more appropriate, allowing better vaporization and mixing of the fuel in the oxidizing stream. An exception to the general trend occurred in the first test of the campaign, F8_001, where the ignition occurred later than expected, due to the very unfavourable O/F value and the initial high G_{ox}. Generally, the oxidizer-to-fuel ratio has a strong influence on the combustion reactions, both in the transient phase of the flame ignition and in the nominal operating phase. Efficiency is also dependent on the O/F ratio; however, in the performed experiments, higher mixture ratios were also related to shorter fuel grains and smaller port volumes, thus further contributing to the final results.

Regarding the second objective of the test campaign, i.e., the possible use of low swirl numbers down to 0.5, the results are encouraging. The tests with HDPE, with a longer grain and no droplet entrainment, showed very high efficiency at small scale. This proves the possibility of using moderately low values of swirl numbers in order to boost the efficiency considerably without an excessive increase in the regression rate, although this finding was not replicated as equally well in the subsequent tests with the F5 paraffin formulation, probably again due to shorter grain and combustion chamber lengths. Adding a post-chamber increased the performance by few percent, as expected from the CFD analyses. A benefit has been also observed in operating at lower oxidizer fluxes, i.e., larger port volumes. It is again expected that larger (and more useful from an application perspective) scales should provide better results. The use of low swirl numbers with a conventional fuel is optimal on the other side of the spectrum compared with the previously mentioned case, i.e., this time at lower scales and long burning times, where high efficiency values remain paramount but the regression rate is kept at moderate levels. In the intermediate range of scales and burning times, more solutions overlap, like higher regressing fuels with lower swirl numbers and lower regressing fuels with higher swirl numbers. The final choice will be thus dictated by other affected aspects like nozzle erosion and blocking, injector size and pressure drop, fuel thermo-mechanical properties and so on. In any case, the combination of all test campaigns proved the third stated goal of the work, the

possibility of playing with two different design variables in order to properly optimize the grain and chamber geometries for a wide range of possible different mission requirements, spanning large variations in size, burning times and motor envelopes, always keeping high performance levels.

A relation that was not specifically studied but was inferred from the data is the one between the regression rate and the average G_{ox} value of the tests. In particular, for identical fuel type and SN_g, experiments with lower average G_{ox}, that is, with larger average fuel port diameters, measure a comparably higher regression value, as shown in Figure 15. The effect is related to the progression of the port diameter during firing, or, more specifically, the time-varying ratio of $\Phi_{port}/\Phi_{injection}$, and this was confirmed for all three types of fuel used. The inferred a constant calculated with the procedure shown earlier shifts slightly upward as $\Phi_{port}/\Phi_{injection}$ increases. This occurrence may explain why pressure graphs (especially those with longer durations) indicate slightly growing pressure in the chamber, which correlates with an n exponent <0.5 and should be examined further in future investigations. Thus, this phenomenon must be considered when designing hybrid motors with long burning times, where the diameter of the grain port may vary greatly between the ignition and the tail off, while the injection diameter remains constant.

During the design phase of the PHAEDRA program, Avio established the requirements for the DEMO test-bed, including a minimum efficiency threshold, a target regression rate level, and the number and timing of the re-ignitions. These parameters are fulfilled by a proper combination between the tested paraffin blends and swirl numbers. The target O/F is then achieved by adjusting the length of the fuel grain accordingly.

The next step of the PHAEDRA program will be the testing of the 7.5 kN DEMO test-bed with the selected configuration to validate all predictions and confirm the fulfillment of the target performance goals.

Figure 16 provides a qualitative summary of the main outcomes reported in this article.

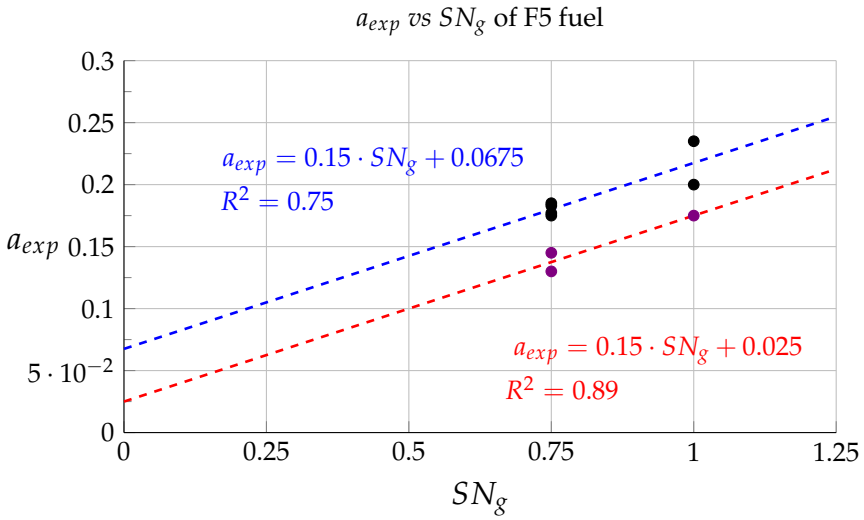

Figure 15. Plotting the values of the a_{exp} constant versus the associated SN_g. Experimental points with an average G_{ox} value greater than 80 kg/m^{2}s are highlighted in violet. Black dots correspond to experimental values with an average oxidizer mass flux values between 20 and 60 kg/m^{2}s. The graph illustrates the equations of the blue and red dashed lines, which are the least squares lines computed considering, respectively, the black and the violet experimental dots.

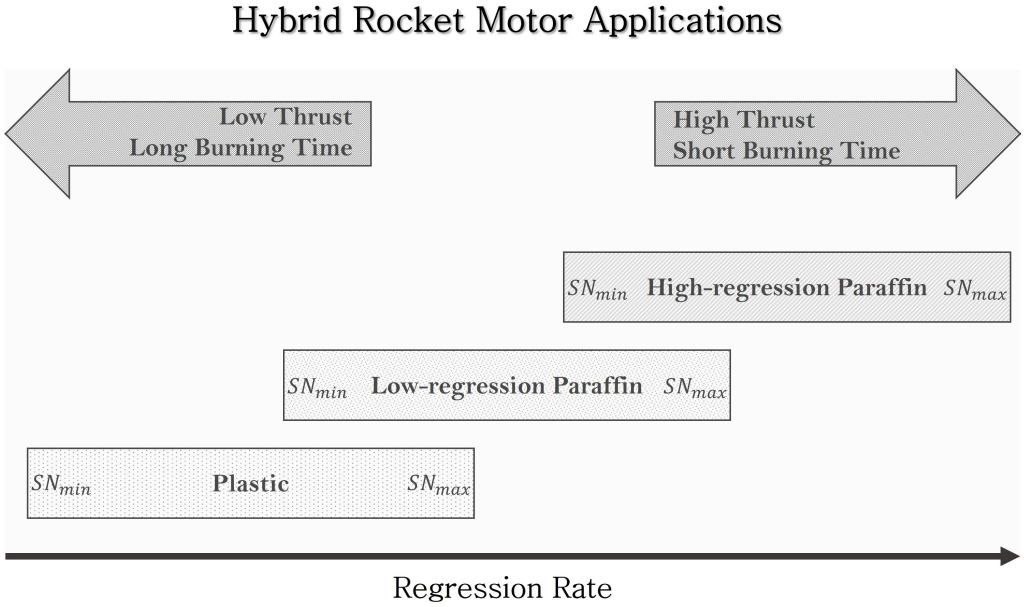

Figure 16. The graphic illustrates how different mission profiles commonly encountered in space applications may be accomplished by hybrid motor technology. In particular, it relates them to the values of regression rates achieved by coupling different types of fuels with different swirl number values. The potential of selecting alternative configurations for the same regression rate values is shown by the overlaps between different fuel compositions.

5. Conclusions

The PHAEDRA program, funded by the Italian Space Agency, aims at improving the understanding and the technology readiness level of hybrid propulsion, with a specific focus on paraffin-based fuels and re-ignitability. The final target is the development and testing of a medium size, scaled-down demonstrator (DEMO) of a reference larger upper stage motor using hydrogen peroxide as an oxidizer. In the frame of this program, a series of preliminary tests campaigns have been performed at lab-scale in order to characterize the behavior of different paraffin blends and vortex injections.

In the first campaign, a strengthened paraffin has been tested with swirl numbers from 0 (axial) to 3.33, showing regression rates up to 15 times higher than classical ones. These notable regression rates are ideal for single port boosters' applications at larger scales and/or shorter burning times than previously considered. Vortex injection provides also high efficiencies (>90%) even at the very small chamber volumes tested, with the expectation to obtain further improvements at the scales of real applications.

In the second campaign, swirl numbers lower than previously investigated have been tested with a conventional plastic fuel, i.e., HDPE. The results confirmed the possibility of raising combustion efficiency to optimal values (>96%) without excessive increase in heat transfer, limiting the effect on the regression rate and nozzle erosion. This combination is instead ideal for smaller sizes and/or longer burning times. Therefore, the two campaigns together proved the possibility of extending the range of applications where hybrid rockets can perform effectively.

The final test campaign combined the low swirl numbers with another paraffin blend loaded with more additives and was able to provide an intermediate regression rate between the plastic fuel and the baseline paraffin. The results confirmed the findings obtained with HDPE, even if with slightly lower efficiencies (generally > 93%), again with the expectation that the results should improve at the targeted sizes.

Concluding, the combination of all the test campaigns have proven the possibility of using two different design variables, namely the swirl number and fuel composition, to optimize hybrid rocket performance and envelope in a wide range of different scenarios.

Moreover, the explored range of combinations between swirl numbers and paraffin types should allow the possibility of fulfilling the requirements set by Avio for the reference upper stage motor and the corresponding scaled-down DEMO test-bed. However, this expectation has to be confirmed by following tests at the increased scale.

Author Contributions: Conceptualization, M.S. and F.B.; Writing, M.S. and F.B.; Resources (paraffin grains), C.P. and L.G., Investigation, M.S., L.Z. and L.N.; Software (CFD), M.T.M., M.F., D.B. and F.N.; Project administration, A.C. and N.B.; Supervision, D.P., R.C.P. and E.C. All authors have read and agreed to the published version of the manuscript.

Funding: This research was funded by Agenzia Spaziale Italiana, grant: 2019-5-I.0.

Data Availability Statement: The datasets presented in this article are not readily available because the data are classified within the PHAEDRA Consortium. Requests to access the datasets should be directed to the Italian Space Agency.

Conflicts of Interest: The authors declare no conflicts of interest.

Abbreviations

The following abbreviations are used in this manuscript:

ASI	Agenzia Spaziale Italiana (Italian Space Agency)
CEA	Chemical Equilibrium with Applications
CFD	Computational fluid dynamics
CV	Cavitating Venturi
HDPE	High-density polyethylene
HRE	Hybrid rocket engine
HTP	High-test peroxide
MEOP	Maximum expected operating pressure
NASA	National Aeronautics and Space Administration
O/F	Oxidizer-to-fuel ratio
PC	Post chamber
PHAEDRA	Paraffinic Hybrid Advanced Engine Demonstrator for Rocket Application
SN	Swirl number
SN_g	Swirl number (geometric)
TP	Thermal protection

References

1. Chiaverini, M. Review of solid-fuel regression rate behavior in classical and nonclassical hybrid rocket motors. *Prog. Astronaut. Aeronaut.* **2007**, *218*, 37.
2. Altman, D.; Holzman, A. Overview and history of hybrid rocket propulsion. *Prog. Astronaut. Aeronaut.* **2007**, *218*, 1.
3. Story, G.; Abel, T.; Claflin, S.; Park, O.; Arves, J.; Kearney, D. Hybrid propulsion demonstration program 250K hybrid motor. In Proceedings of the 39th AIAA/ASME/SAE/ASEE Joint Propulsion Conference and Exhibit, Huntsville, Alabama, 20–23 July 2003; p. 5198.
4. Story, G.; Arves, J. Flight Testing of Hybrid Powered Vehicles. In *Fundamentals of Hybrid Rocket Combustion and Propulsion*; American Institute of Aeronautics and Astronautics: Reston, VA, USA, 2007; pp. 553–592.
5. Kobald, M.; Fischer, U.; Tomilin, K.; Petrarolo, A.; Kysela, P.; Schmierer, C.; Pahler, A.; Gauger, J.; Breitinger, J.; Hertel, F.; et al. Sounding Rocket" HEROS"-A Low-Cost Hybrid Rocket Technology Demonstrator. In Proceedings of the 53rd AIAA/SAE/ASEE Joint Propulsion Conference, Atlanta, GA, USA, 10–12 July 2017; p. 4902.
6. Karabeyoglu, A.; Stevens, J.; Geyzel, D.; Cantwell, B.; Micheletti, D. High performance hybrid upper stage motor. In Proceedings of the 47th AIAA/ASME/SAE/ASEE Joint Propulsion Conference & Exhibit, San Diego, CA, USA, 31 July–3 August 2011; p. 6025.
7. Schmierer, C.; Kobald, M.; Tomilin, K.; Fischer, U.; Schlechtriem, S. Low cost small-satellite access to space using hybrid rocket propulsion. *Acta Astronaut.* **2019**, *159*, 578–583. [CrossRef]
8. Mazzetti, A.; Merotto, L.; Pinarello, G. Paraffin-based hybrid rocket engines applications: A review and a market perspective. *Acta Astronaut.* **2016**, *126*, 286–297. [CrossRef]
9. Ruffin, A.; Paccagnella, E.; Santi, M.; Barato, F.; Pavarin, D. Real-time deep throttling tests of a hydrogen peroxide hybrid rocket motor. *J. Propuls. Power* **2022**, *38*, 833–848. [CrossRef]

10. Barato, F.; Toson, E.; Pavarin, D. Variations and control of thrust and mixture ratio in hybrid rocket motors. *Adv. Astronaut. Sci. Technol.* **2021**, *4*, 55–76. [CrossRef]
11. Ruffin, A.; Santi, M.; Paccagnella, E.; Barato, F.; Bellomo, N.; Miste, G.A.; Venturelli, G.M.; Pavarin, D. Development of a flow control valve for a throttleable hybrid rocket motor and throttling fire tests. In Proceedings of the 2018 Joint Propulsion Conference, Cincinnati, OH, USA, 9–11 July 2018; p. 4664.
12. Okninski, A.; Kopacz, W.; Kaniewski, D.; Sobczak, K. Hybrid rocket propulsion technology for space transportation revisited-propellant solutions and challenges. *FirePhysChem* **2021**, *1*, 260–271. [CrossRef]
13. Glaser, C.; Hijlkema, J.; Anthoine, J. Bridging the Technology Gap: Strategies for Hybrid Rocket Engines. *Aerospace* **2023**, *10*, 901. [CrossRef]
14. Okninski, A.; Surmacz, P.; Bartkowiak, B.; Mayer, T.; Sobczak, K.; Pakosz, M.; Kaniewski, D.; Matyszewski, J.; Rarata, G.; Wolanski, P. Development of green storable hybrid rocket propulsion technology using 98% hydrogen peroxide as oxidizer. *Aerospace* **2021**, *8*, 234. [CrossRef]
15. Kuo, K.K. Challenges of hybrid rocket propulsion in the 21st century. *Fundam. Hybrid Rocket. Combust. Propuls.* **2007**, *18*, 593–638.
16. Pastrone, D. Approaches to low fuel regression rate in hybrid rocket engines. *Int. J. Aerosp. Eng.* **2012**, *2012*, 649753. [CrossRef]
17. Carmicino, C.; Orlandi, O.; Sorge, A.; Dauch, F.; De Amicis, R.; de Rosa, M. Basic aspects of the hybrid engine operation. In Proceedings of the 45th AIAA/ASME/SAE/ASEE Joint Propulsion Conference & Exhibit, Denver, CO, USA, 2–5 August 2009; p. 4937.
18. Karabeyoglu, A.; Zilliac, G.; Cantwell, B.J.; DeZilwa, S.; Castellucci, P. Scale-up tests of high regression rate paraffin-based hybrid rocket fuels. *J. Propuls. Power* **2004**, *20*, 1037–1045. [CrossRef]
19. Karabeyoglu, M.; Altman, D.; Cantwell, B.J. Combustion of liquefying hybrid propellants: Part 1, general theory. *J. Propuls. Power* **2002**, *18*, 610–620. [CrossRef]
20. Karabeyoglu, M.; Cantwell, B.J. Combustion of liquefying hybrid propellants: Part 2, stability of liquid films. *J. Propuls. Power* **2002**, *18*, 621–630. [CrossRef]
21. Barato, F.; Bellomo, N.; Lazzarin, M.; Moretto, F.; Bettella, A.; Pavarin, D. Numerical modeling of paraffin-based fuels behavior. In Proceedings of the 48th AIAA/ASME/SAE/ASEE Joint Propulsion Conference & Exhibit, Atlanta, GA, USA, 30 July–1 August 2012; p. 3750.
22. Paccagnella, E.; Santi, M.; Ruffin, A.; Barato, F.; Pavarin, D.; Misté, G.A.; Venturelli, G.; Bellomo, N. Testing of a long-burning-time paraffin-based hybrid rocket motor. *J. Propuls. Power* **2019**, *35*, 432–442. [CrossRef]
23. Karabeyoglu, A.; Cantwell, B.; Stevens, J. Evaluation of the homologous series of normal alkanes as hybrid rocket fuels. In Proceedings of the 41st AIAA/ASME/SAE/ASEE Joint Propulsion Conference & Exhibit, Tucson, AZ, USA, 10–13 July 2005; p. 3908.
24. Marxman, G.; Wooldridge, C.; Muzzy, R. Fundamentals of hybrid boundary-layer combustion. In *Progress in Astronautics and Rocketry*; Elsevier: Amsterdam, The Netherlands, 1964; Volume 15, pp. 485–522.
25. Netzer, D.W.; Bae, W.E. *Hybrid Rocket Internal Ballistics*; Chemical Propulsion Information Agency: Laurel, MD, USA, 1972.
26. Marquardt, T.; Majdalani, J. Review of classical diffusion-limited regression rate models in hybrid rockets. *Aerospace* **2019**, *6*, 75. [CrossRef]
27. Galfetti, L.; Merotto, L.; Boiocchi, M.; Maggi, F.; DeLuca, L. Experimental investigation of paraffin-based fuels for hybrid rocket propulsion. *Prog. Propuls. Phys.* **2013**, *4*, 59–74.
28. Paravan, C.; Galfetti, L.; Maggi, F. A critical analysis of paraffin-based fuel formulations for hybrid rocket propulsion. In Proceedings of the 53rd AIAA/SAE/ASEE Joint Propulsion Conference, Atlanta, GA, USA, 10–12 July 2017; p. 4830.
29. Weinstein, A.; Gany, A. Investigation of Paraffin-based Fuels in hybrid Combustors. *Int. J. Energetic Mater. Chem. Propuls.* **2011**, *10*, 277–296. [CrossRef]
30. Mechentel, F.S.; Cantwell, B.J. Experimental findings on pre-and post-combustion chamber effects in a laboratory-scale motor. In Proceedings of the AIAA Propulsion and Energy 2019 Forum, Indianapolis, IN, USA, 19–22 August 2019; p. 4336.
31. Bettella, A.; Lazzarin, M.; Bellomo, N.; Barato, F.; Pavarin, D.; Grosse, M. Testing and CFD simulation of diaphragm hybrid rocket motors. In Proceedings of the 47th AIAA/ASME/SAE/ASEE Joint Propulsion Conference & Exhibit, San Diego, CA, USA, 31 July–3 August 2011; p. 6023.
32. Bellomo, N.; Lazzarin, M.; Barato, F.; Bettella, A.; Pavarin, D.; Grosse, M. Investigation of effect of diaphragms on the efficiency of hybrid rockets. *J. Propuls. Power* **2014**, *30*, 175–185. [CrossRef]
33. Grosse, M. Effect of a diaphragm on performance and fuel regression of a laboratory scale hybrid rocket motor using nitrous oxide and paraffin. In Proceedings of the 45th AIAA/ASME/SAE/ASEE Joint Propulsion Conference & Exhibit, Denver, CO, USA, 2–5 August 2009; p. 5113.
34. Yuasa, S.; Shimada, O.; Imamura, T.; Tamura, T.; Yamoto, K. A technique for improving the performance of hybrid rocket engines. In Proceedings of the 35th Joint Propulsion Conference and Exhibit, Los Angeles, CA, USA, 20–24 June 1999; p. 2322.
35. Takashi, T.; Yuasa, S.; Yamamoto, K. Effects of swirling oxidizer flow on fuel regression rate of hybrid rockets. In Proceedings of the 35th Joint Propulsion Conference and Exhibit, Los Angeles, CA, USA, 20–24 June 1999; p. 2323.
36. Jones, C.; Myre, D.; Cowart, J. Performance and analysis of vortex oxidizer injection in a hybrid rocket motor. In Proceedings of the 45th AIAA/ASME/SAE/ASEE Joint Propulsion Conference & Exhibit, Denver, CO, USA, 2–5 August 2009; p. 4938.

37. Knuth, W.; Chiaverini, M.; Gramer, D.; Sauer, J. Experimental investigation of a vortex-driven high-regression rate hybrid rocket engine. In Proceedings of the 34th AIAA/ASME/SAE/ASEE Joint Propulsion Conference and Exhibit, Cleveland, OH, USA, 13–15 July 1998; p. 3348.
38. Paccagnella, E.; Barato, F.; Pavarin, D.; Karabeyoğlu, A. Scaling parameters of swirling oxidizer injection in hybrid rocket motors. *J. Propuls. Power* **2017**, *33*, 1378–1394. [CrossRef]
39. Paccagnella, E.; Barato, F.; Pavarin, D.; Karabeyoglu, A.M. Scaling of hybrid rocket motors with swirling oxidizer injection-Part 2. In Proceedings of the 52nd AIAA/SAE/ASEE Joint Propulsion Conference, Salt Lake City, UT, USA, 25–27 July 2016; p. 4750.
40. Bellomo, N.; Barato, F.; Faenza, M.; Lazzarin, M.; Bettella, A.; Pavarin, D. Numerical and experimental investigation of unidirectional vortex injection in hybrid rocket engines. *J. Propuls. Power* **2013**, *29*, 1097–1113. [CrossRef]
41. Gupta, A.K.; Lilley, D.G.; Syred, N. *Swirl Flows*; Abacus Press: Tunbridge Wells, England, 1984; ISBN 978-0996100427
42. Toson, E.; Karabeyoglu, A.M. Design and optimization of hybrid propulsion systems for in-space application. In Proceedings of the 51st AIAA/SAE/ASEE Joint Propulsion Conference, Orlando, FL, USA, 27–29 July 2015; p. 3937.
43. Barato, F.; Paccagnella, E.; Pavarin, D. Explicit analytical equations for single port hybrid rocket combustion chamber sizing. *J. Propuls. Power* **2020**, *36*, 869–886. [CrossRef]
44. Barato, F. Challenges of Ablatively Cooled Hybrid Rockets for Satellites or Upper Stages. *Aerospace* **2021**, *8*, 190. [CrossRef]
45. Franco, M.; Barato, F.; Paccagnella, E.; Santi, M.; Battiston, A.; Comazzetto, A.; Pavarin, D. Regression rate design tailoring through vortex injection in hybrid rocket motors. *J. Spacecr. Rocket.* **2020**, *57*, 278–290. [CrossRef]
46. Rampazzo, A.; Barato, F. Modeling and CFD Simulation of Regression Rate in Hybrid Rocket Motors. *Fire* **2023**, *6*, 100. [CrossRef]
47. Bianchi, D.; Leccese, G.; Nasuti, F.; Onofri, M.; Carmicino, C. Modeling of high density polyethylene regression rate in the simulation of hybrid rocket flowfields. *Aerospace* **2019**, *6*, 88. [CrossRef]
48. Leccese, G.; Bianchi, D.; Nasuti, F. Modeling and Simulation of Paraffin–Based Hybrid Rocket Internal Ballistics. In Proceedings of the 2018 Joint Propulsion Conference, Cincinnati, OH, USA, 9–11 July 2018; p. 4533.
49. Di Martino, G.D.; Carmicino, C.; Mungiguerra, S.; Savino, R. The application of computational thermo-fluid-dynamics to the simulation of hybrid rocket internal ballistics with classical or liquefying fuels: A review. *Aerospace* **2019**, *6*, 56. [CrossRef]
50. Migliorino, M.T.; Fabiani, M.; Bianchi, D.; Nasuti, F.; Barato, F.; Bellomo, N.; Pavarin, D.; Pizzurro, S.; Pizzarelli, M.; Pellegrini, R.C.; et al. Numerical Simulations of a Paraffin-Hydrogen Peroxide Hybrid Rocket with Swirl Injection. In Proceedings of the AIAA SCITECH 2023 Forum, National Harbor, MD, USA, 23–27 January 2023; p. 2350.
51. Motoe, M.; Shimada, T. Numerical simulations of combustive flows in a swirling-oxidizer-flow-type hybrid rocket. In Proceedings of the 52nd Aerospace Sciences Meeting, National Harbor, MD, USA, 13–17 January 2014; p. 310.
52. Cheng, G.; Farmer, R.; Jones, H.; McFarlane, J. Numerical simulation of the internal ballistics of a hybrid rocket motor. In Proceedings of the 32nd Aerospace Sciences Meeting and Exhibit, Reno, NV, USA, 10–13 January 1994; p. 554.
53. Syred, N.; Beer, J. Combustion in swirling flows: A review. *Combust. Flame* **1974**, *23*, 143–201. [CrossRef]
54. Reina, A.; Frezzotti, M.; Mangioni, G.; Cretella, A.; Battista, F.; Paravan, C.; Nasuti, F.; Pavarin, D.; Pellegrini, R.; Cavallini, E.; et al. Hybrid propulsion system for future rocket applications. In Proceedings of the Space Propulsion Conference, Estoril, Portugal, 9–13 May 2022; pp. 1–11.
55. Karabeyoglu, A. Challenges in the development of large-scale hybrid rockets. *Int. J. Energetic Mater. Chem. Propuls.* **2017**, *16*. [CrossRef]
56. Hopkins, J.; Skinner, M.; Buchanan, A.; Gulman, R. Overview of a 4-inch OD Paraffin-Based Hybrid Sounding Rocket Program In Proceedings of the 40th AIAA/ASME/SAE/ASEE Joint Propulsion Conference and Exhibit, Fort Lauderdale, FL, USA, 11–14 July 2004.
57. Randall, L. Rocket applications of the cavitating venturi. *J. Am. Rocket. Soc.* **1952**, *22*, 28–38.

Disclaimer/Publisher's Note: The statements, opinions and data contained in all publications are solely those of the individual author(s) and contributor(s) and not of MDPI and/or the editor(s). MDPI and/or the editor(s) disclaim responsibility for any injury to people or property resulting from any ideas, methods, instructions or products referred to in the content.